Supporting Information for "A Roadmap for Simulating Chemical Dynamics on a Parametrically Driven Bosonic Quantum Device"

Delmar G. A. Cabral,[†,#] Pouya Khazaei,[‡,#] Brandon C. Allen,[†,#] Pablo E. Videla,[†,#] Max Schäfer,[¶,§] Rodrigo G. Cortiñas,[¶,§] Alejandro Cros Carrillo de Albornoz,[¶,§,‖] Jorge Chávez-Carlos,[⊥] Lea F. Santos,[⊥] Eitan Geva,[*,‡] and Victor S. Batista[*,†,§]

†*Department of Chemistry, Yale University, New Haven, CT 06520, USA*

‡*Department of Chemistry, University of Michigan, Ann Arbor, MI 48109, USA*

¶*Department of Applied Physics and Physics, Yale University, New Haven, CT 06520, USA*

§*Yale Quantum Institute, Yale University, New Haven, CT 06511, USA*

‖*Department of Physics and Astronomy, University College London, London WC1E 6BT, UK*

⊥*Department of Physics, University of Connecticut, Storrs, CT 06511, USA*

#*Contributed equally to this work*

E-mail: eitan@umich.edu; victor.batista@yale.edu

Mapping the Device Hamiltonian to Chemical Double-Well

We start out by considering the following general Hamiltonian which is suitable for modeling the dynamics of a wide range of elementary chemical reactions:

$$\hat{H}_{DW} = \frac{\hat{p}^2}{2m} + k_4\hat{x}^4 - k_2\hat{x}^2 + k_1\hat{x} \quad . \tag{1}$$

Here, $\hat{x}$ and $\hat{p}$ are the position and momentum operators associated with motion along the reaction coordinate, which satisfy $[\hat{x}, \hat{p}] = i\hbar$; m is the mass associated with the motion along the reaction coordinate; and $\{k_1, k_2, k_4\}$ are positive and real parameters whose values define the double well free energy profile, and thereby the specific chemical system, that the Hamiltonian describes. More specifically, given the double-well free energy profile for a specific chemical system, which can be obtained from electronic structure and MD simulations,[1] we assume that it can be fitted to a minimal fourth-order polynomial of the form $V(x) = k_4x^4 - k_2x^2 + k_1x$. The $k_4x^4 - k_2x^2$ term is necessary for obtaining the double-well feature, while the k_1x term is necessary in order to account for asymmetry between the reactant and product wells ($k_1 = 0$ gives rise to a symmetrical double-well free energy profile, which corresponds to an iso-energetic chemical reaction for which $\Delta G = 0$). It should be noted that a third order x^3 term is excluded. This is necessary for mapping onto the Hamiltonian of currently accessible experimental Kerr-cat devices (see below), and justified by the fact that adding a x^3 term is not necessary for capturing the main features associated with a chemical reaction, namely an asymmetrical double-well profile. It should also be noted that a description of the chemical dynamics in terms of a TST/Arrhenius-like rate constant requires coupling the reaction coordinate to a thermal bath of nonreactive DOF in order to make activation to the transition state and barrier crossing possible, followed by equilibration in the product well before significant recrossing can occur (see below). We consider the

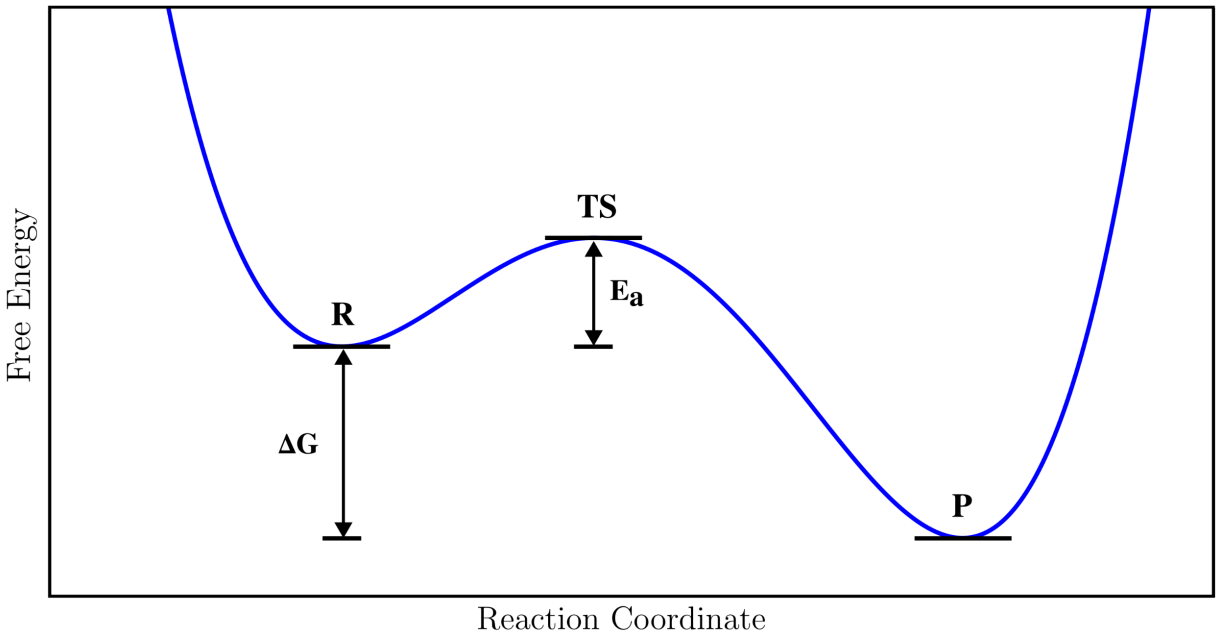

Figure 1: A schematic view of the the free energy double-well profile, $V(x)$, along the reaction coordinate, x. The reactant and product wells are designated by R and P, respectively. The transition state, which corresponds to the barrier top, is designated by TS. E_a and ΔG are the activation energy and reaction free energy, respectively. It should be noted that the reaction coordinate needs to be coupled to a thermal bath of nonreactive DOF (not shown) in order for rate kinetics to be emerge.

effective Hamiltonian for currently experimentally realizable parametrically-driven Kerr-cat cQED devices, which is given by:[2–7]

$$\hat{H}_{KC} = \Delta \hat{a}^\dagger \hat{a} - K(\hat{a}^\dagger)^2(\hat{a})^2 + \epsilon_2(\hat{a}^2 + \hat{a}^{\dagger 2}) + \epsilon_1(\hat{a} + \hat{a}^\dagger) \quad . \tag{2}$$

Here, $\hat{a}$ and $\hat{a}^\dagger$ are (unit-less) photonic creation and annihilation operators associated with the electromagnetic mode supported by the cavity, which satisfy $[\hat{a}, \hat{a}^\dagger] = \hat{1}$, and $\{\Delta, K, \epsilon_2, \epsilon_1\}$ are experimentally controllable parameters (all given in terms of energy units). Noting that the double-well and Kerr-cat Hamiltonians in Eqs. (1) and (2), respectively, are both given by fourth-order polynomials determined by four free parameters ($\{m, k_1, k_2, k_4\}$ and $\{\Delta, K, \epsilon_2, \epsilon_1\}$, respectively), our goal in the next step is to map the Kerr-cat Hamiltonian in Eq. (2), onto the chemical double-well Hamiltonian in Eq. (1).

To this end, we first need to map the photonic operators, $\{\hat{a}, \hat{a}^\dagger\}$ onto the operators associated with motion along the reaction coordinate, $\{\hat{x}, \hat{p}\}$. To generate the correct dynamics, the mapping needs to be consistent with the corresponding commutators: $[\hat{x}, \hat{p}] = i\hbar$ and $[\hat{a}, \hat{a}^\dagger] = \hat{1}$. A mapping that satisfies this is given by:

$$\begin{aligned} \hat{a} &= \frac{1}{\sqrt{2}}\left(\frac{1}{c}\hat{x} + \frac{ic}{\hbar}\hat{p}\right) \quad ; \quad \hat{a}^\dagger = \frac{1}{\sqrt{2}}\left(\frac{1}{c}\hat{x} - \frac{ic}{\hbar}\hat{p}\right) \\ \hat{x} &= \frac{c}{\sqrt{2}}\left(\hat{a} + \hat{a}^\dagger\right) \quad ; \quad \hat{p} = \frac{\hbar}{i\sqrt{2}c}\left(\hat{a} - \hat{a}^\dagger\right) \quad . \end{aligned} \tag{3}$$

Here, c is a constant parameter that has units of length (same units as $\hat{x}$). Importantly, the value of c is arbitrary in the sense that the commutators $[\hat{x}, \hat{p}] = i\hbar$ and $[\hat{a}, \hat{a}^\dagger] = \hat{1}$ are invariant to the choice of c. In other words, the mapping of $\{\hat{a}, \hat{a}^\dagger\}$ onto $\{\hat{x}, \hat{p}\}$ is not unique. As we will see below, this flexibility with respect to the choice of c plays an crucial role in mapping the Kerr-cat Hamiltonian in Eq. (2), onto the chemical double-well Hamiltonian in Eq. (1).

Substituting the expressions for $\hat{a}$ and $\hat{a}^\dagger$ in terms of $\hat{x}$ and $\hat{p}$ from Eq. (3) into Eq. (2),

we can recast the *negative* of the Kerr-cat Hamiltonian in terms of the $\hat{x}$ and $\hat{p}$ (dropping constant terms which do not impact the dynamics):

$$-\hat{H}_{KC} = \frac{c^2}{\hbar^2}\left(\epsilon_2 - K - \Delta/2\right)\hat{p}^2 + \frac{K}{4c^4}\hat{x}^4 - \frac{1}{c^2}\left(\epsilon_2 + K + \Delta/2\right)\hat{x}^2 - \frac{\epsilon_1\sqrt{2}}{c}\hat{x} + \frac{Kc^4}{4\hbar^4}\hat{p}^4 + \frac{K}{4\hbar^2}\hat{x}^2\hat{p}^2 + \frac{K}{4\hbar^2}\hat{p}^2\hat{x}^2 \tag{4}$$

Comparing Eq. (4) with Eq. (1), we see that while $-\hat{H}_{KC}$ contains $\hat{p}^2$, $\hat{x}^4$, $\hat{x}^2$ and $\hat{x}$ terms which can be mapped onto the corresponding terms in the chemical double-well Hamiltonian in Eq. (1), it also contains spurious $\hat{p}^4$, $\hat{x}^2\hat{p}^2$ and $\hat{p}^2\hat{x}^2$ terms that lack counterparts in Eq. (1).

In the next step, we map $\{\Delta, K, \epsilon_2, \epsilon_1\}$ onto $\{m, k_1, k_2, k_4\}$ by requiring consistency between the $\hat{p}^2$, $\hat{x}^4$, $\hat{x}^2$ and $\hat{x}$ terms in Eqs. (1) and (4), which leads to the following mapping relations:

$$K = 4c^4 k_4 \tag{5}$$

$$\epsilon_2 = \frac{\hbar^2 + 2c^4 k_2 m}{4c^2 m} \tag{6}$$

$$\Delta = \frac{2c^4 k_2 m - \hbar^2 - 16c^6 k_4 m}{2c^2 m} \tag{7}$$

$$\epsilon_1 = -\frac{c k_1}{\sqrt{2}} \tag{8}$$

We also take advantage of the aforementioned flexibility in choosing the value of c to minimize the effect of the spurious $\hat{p}^4$, $\hat{x}^2\hat{p}^2$ and $\hat{p}^2\hat{x}^2$ terms in Eq. (1). As we show below, doing so requires that we choose a value of c small enough so that it satisfies the following inequality:

$$\frac{\hbar^2}{m k_2 c^4} \gg 1 \tag{9}$$

To derive the inequality in Eq. (9), we note that the $\hat{x}^4$, $\hat{x}^2$ and $\hat{x}$ terms in Eq. (4) become *larger* relative to the other terms with *decreasing* c. This suggests that choosing

a sufficiently small value of c can make the spurious p^4, x^2p^2 and x^2p^2 terms negligible. However, the fact the kinetic energy term in Eq. (4), $\frac{c^2}{\hbar^2}\left(\epsilon_2 - K - \Delta/2\right)\hat{p}^2$, also decreases with decreasing c implies that the value of c also needs to be chosen such that the spurious terms will be negligible compared to it. It must be noted that if one puts Eq. 5-8 in units of K, that being $\{\epsilon_1/K, \epsilon_2/K, \Delta/K\}$, these quantities diverge when $\lim c \to 0$, with these quantities getting quite large when c is small. So, it is necessary to pick a value of c which produces experimentally accessible values of $\{\epsilon_1/K, \epsilon_2/K, \Delta/K\}$ for a given chemical system while ensuring sufficient chemical accuracy.

To this end, we consider the the symmetrical double-well case ($k_1 = 0$), for which it can be shown that the reactant and product equilibrium geometries are given by $\pm x_0$, where $x_0 = \sqrt{\frac{k_2}{2k_4}}$ and the activation energy is given by $E_a = \frac{k_2^2}{4k_4}$. Thus, $\{x_0, E_a\}$ are interchangeable with $\{k_2, k_4\}$ in this case, such that Eq. (5) becomes $K = \frac{4E_a c^4}{x_0^4}$. Hence,

$$\frac{K}{4\hbar^2}\left[\frac{c^4}{\hbar^2}\hat{p}^4 + \hat{x}^2\hat{p}^2 + \hat{p}^2\hat{x}^2\right] \to \frac{E_a c^4}{\hbar^2 x_0^4}\left[\frac{c^4}{\hbar^2}\hat{p}^4 + \hat{x}^2\hat{p}^2 + \hat{p}^2\hat{x}^2\right] \tag{10}$$

Given that x_0 set the length scale of the chemical system, one can estimate the order of magnitude of the $\hat{x}^2\hat{p}^2$ and $\hat{p}^2\hat{x}^2$ terms to be $\frac{E_a c^4}{\hbar^2 x_0^4} x_0^2 \hat{p}^2 = \frac{E_a c^4}{\hbar^2 x_0^2}\hat{p}^2$. Thus, requiring that the spurious $\hat{x}^2\hat{p}^2$ and $\hat{p}^2\hat{x}^2$ terms are negligible relative to the kinetic energy term, $\frac{\hat{p}^2}{2m}$ gives rise to the inequality $\frac{E_a c^4}{\hbar^2 x_0^2}\hat{p}^2 \ll \frac{1}{2m}\hat{p}^2$, which can be rearranged to give $\frac{\hbar^2 x_0^2}{2mE_a c^4} \gg 1$. Noting that $k_2 = \frac{2E_a}{x_0^2}$ then leads to the inequality in Eq. (9).

The fact that the $\hat{p}^4$ term scales like c^4, while the $\hat{p}^2$ term scales like c^2, also implies that the $\hat{p}^4$ will become negligible for a sufficiently small value of c. In fact, the same inequality, Eq. (9), can be derived by noting that $\frac{1}{2m}\hat{p}^2 \gg \frac{E_a c^8}{\hbar^4 x_0^4}\hat{p}^4$ is equivalent to $\frac{1}{2m} \gg \frac{E_a c^8}{\hbar^4 x_0^4}\hat{p}^2$ and that the momentum is maximal when the particle is around the minima, where the potential energy can be approximated as being harmonic. Invoking the virial theorem for the harmonic oscillator, according to which the expectation values of the kinetic energy is equal to that of the potential energy, and noting that E_a sets the potential energy scale for the chemical

system, we can then estimate $\hat{p}^2$ by $2mE_a$ in the inequality $\frac{1}{2m} \gg \frac{E_a c^8}{\hbar^4 x_0^4}\hat{p}^2$, which turns it into the inequality $\left(\frac{\hbar^2 x_0^2}{2mE_a c^4}\right)^2 \gg 1$. Thus, satisfying the inequality in Eq. (9), which is equivalent to $\frac{\hbar^2 x_0^2}{2mE_a c^4} \gg 1$, also guarantees that the $\hat{p}^4$ term will becomes negligible compared the the $\hat{p}^2$ kinetic energy term.

Finally, the same argument would also hold for an *asymmetrical* double-well since the length and energy scales of the chemical system are not going to be significantly affected by the addition of the asymmetry.

Computational Methods

In this work, we examine the dissipative dynamics of the asymmetric Kerr-cat Hamiltonian,

$$\frac{\hat{H}}{\hbar} = \Delta\hat{a}^\dagger\hat{a} - K(\hat{a}^\dagger)^2(\hat{a})^2 + \epsilon_2(\hat{a}^2 + \hat{a}^{\dagger 2}) + \epsilon_1(\hat{a} + \hat{a}^\dagger), \tag{11}$$

where Δ, ϵ_2, ϵ_1 control the potential landscape parameters such as inter-well separation, barrier height, and well asymmetry, respectively. The entire Hamiltonian is scaled by K, which is taken to be a constant value throughout the manuscript, unless otherwise stated. The operators $a^\dagger, a$ are the quantum Harmonic oscillator excitation and de-excitation operators expressed in the basis of Fock states. To simulate the dissipative dynamics of this Hamiltonian, we use the Lindblad master equation:

$$\frac{\partial\hat{\rho}(t)}{\partial t} = -\frac{i}{\hbar}\left[\hat{H}, \hat{\rho}(t)\right] + \mathcal{D}\left[\hat{\rho}(t)\right], \tag{12}$$

where $\hat{H}$ is the Kerr-cat Hamiltonian, $\hat{\rho}(t)$ is the time-dependent density matrix and $\mathcal{D}[\hat{\rho}(t)]$ is the dissipator defined as:

$$\mathcal{D}[\hat{\rho}(t)] = \kappa(1 + n_{\text{th}})\left(\hat{a}\hat{\rho}\hat{a}^\dagger - \frac{1}{2}\{\hat{a}^\dagger\hat{a}, \hat{\rho}\}\right) + \kappa n_{\text{th}}\left(\hat{a}^\dagger\hat{\rho}\hat{a} - \frac{1}{2}\{\hat{a}\hat{a}^\dagger, \hat{\rho}\}\right) \tag{13}$$

with $a^\dagger, a$ being excitation and deexcitation operators, whose effect is governed by the magnitude of the thermal parameters κ and n_{th}. To implement the Lindblad equation and simulate dissipative dynamics, we vectorize the density matrix and matricize the Lindbladian, using the relationship $\text{vec}(AXB) = (B^T \otimes A)\text{vec}(X)$, such that

$$\frac{\partial \hat{\rho}}{\partial t} = \hat{\mathcal{L}}\hat{\rho} \tag{14}$$

Thus, we must find a suitable representation for $\hat{\mathcal{L}}$. We introduce identity matrices to utilize the vectorization relationship and apply it to the Hamiltonian:

$$\left[\hat{H}, \hat{\rho}(t)\right] = \hat{H}\hat{\rho}\mathbb{I} - \mathbb{I}\hat{\rho}\hat{H} \tag{15}$$

$$= \left(\mathbb{I} \otimes \hat{H} - \hat{H}^T \otimes \mathbb{I}\right)\hat{\rho} \tag{16}$$

Similarly, we can alter the dissipator:

$$\begin{aligned}\mathcal{D}[\hat{\rho}(t)] = \kappa(1+n_{\text{th}})&\left(\hat{a}\hat{\rho}\hat{a}^\dagger - \frac{1}{2}\left(\hat{a}^\dagger\hat{a}\hat{\rho}\mathbb{I} + \mathbb{I}\hat{\rho}\hat{a}^\dagger\hat{a}\right)\right)\\ &+\kappa n_{\text{th}}\left(\hat{a}^\dagger\hat{\rho}\hat{a} - \frac{1}{2}\left(\hat{a}\hat{a}^\dagger\hat{\rho}\mathbb{I} + \mathbb{I}\hat{\rho}\hat{a}\hat{a}^\dagger\right)\right) \qquad (17)\\ = \kappa(1+n_{\text{th}})&\left(\hat{a}^* \otimes \hat{a} - \frac{1}{2}\left(\mathbb{I} \otimes \hat{a}^\dagger\hat{a} + \hat{a}^T\hat{a}^* \otimes \mathbb{I}\right)\right)\hat{\rho}\\ &+\kappa n_{\text{th}}\left(\hat{a}^T \otimes \hat{a}^\dagger - \frac{1}{2}\left(\mathbb{I} \otimes \hat{a}\hat{a}^\dagger + \hat{a}^*\hat{a}^T \otimes \mathbb{I}\right)\right)\hat{\rho} \qquad (18)\end{aligned}$$

Reassembling the complete matricized Lindblad equation, we obtain

$$\begin{aligned}\dot{\hat{\rho}} = \Bigg(&\mathbb{I} \otimes \hat{H} - \hat{H}^T \otimes \mathbb{I}\\ &+ \kappa(1+n_{\text{th}})\left(\hat{a}^* \otimes \hat{a} - \frac{1}{2}\left(\mathbb{I} \otimes \hat{a}^\dagger\hat{a} + \hat{a}^T\hat{a}^* \otimes \mathbb{I}\right)\right)\\ &+ \kappa n_{\text{th}}\left(\hat{a}^T \otimes \hat{a}^\dagger - \frac{1}{2}\left(\mathbb{I} \otimes \hat{a}\hat{a}^\dagger + \hat{a}^*\hat{a}^T \otimes \mathbb{I}\right)\right)\Bigg)\hat{\rho} \qquad (19)\end{aligned}$$

To simulate the population dynamics, we integrate equation 14,

$$\hat{\rho}_t = \hat{\rho}(t) = e^{\hat{\mathcal{L}}t}\hat{\rho}_0 \tag{20}$$

and calculate the action of time-evolution of the Lindbladian operator on the propagated density matrix for a small time-step $\tau = 0.1$:

$$\hat{\rho}(t) = e^{\hat{\mathcal{L}}\tau}\hat{\rho}(t-\tau) \tag{21}$$

The matrix exponential operator is implemented using the `scipy.linalg.expm` routine, which implements a scaling and squaring algorithm based on Pade's approximation.[8]

Initial State

The initial state of the system is crucial to the dynamics. We start by diagonalizing the Hamiltonian H to find the eigenstate matrix Φ of the system in the harmonic oscillator Fock basis:

$$H\Phi = \lambda\Phi \tag{22}$$

We then find the grid-based position representation (x) of the individual eigenstates, ϕ_i, using the quantum Harmonic oscillator basis set:

$$\phi_i = \sum_n^N c_{n,i}\psi_n(x) \tag{23}$$

Where $c_{n,i}$ indicate the expansion coefficients associated with eigenstate i and using N harmonic oscillator functions of the form

$$\psi_n(x) = \frac{1}{\sqrt{2^n\, n!}}\left(\frac{m\omega}{\pi\hbar}\right)^{1/4} e^{-\frac{m\omega x^2}{2\hbar}} H_n\left(\sqrt{\frac{m\omega}{\hbar}}x\right), \qquad n = 0, 1, 2, \ldots \tag{24}$$

In this expression, n indicates the order of the basis function, m represents the mass, ω is the fundamental frequency of the oscillator, $\hbar$ is the reduced Planck's constant and H_n are the physicist's Hermite polynomials of order n, which follow the following recurrence relation:

$$\begin{cases} H_0(x) = 1 \\ H_1(x) = 2x \\ \vdots \\ H_{n+1}(x) = 2xH_n(x) - 2nH_{n-1}(x) \end{cases}$$

We select a suitable initial state by finding the first state with more than 50% amplitude on the desired portion of the potential energy surface (figure 2, left panel) and then convolve it with a sigmoidal filter function of the form:

$$S(x; x_0, t) = \frac{1}{1 + e^{-(x-x_0)/t}}, \tag{25}$$

where x indicates the position, x_0 indicates the cutoff position and t the smoothness of the function near the cutoff. We observe that the Heaviside function, $\Theta(x; x_0) = 1$ if $x \geq x_0$ else $\Theta(x; x_0) = 0$, is recovered when taking $\lim_{t\to 0} S(x; x_0, t)$. This allows localization of the initial state in position space which we then convert back to the Fock basis representation (figure 2, right panel). All dynamics trajectories use eigenstate selection with a sigmoidal filter with a tail of 0.5.

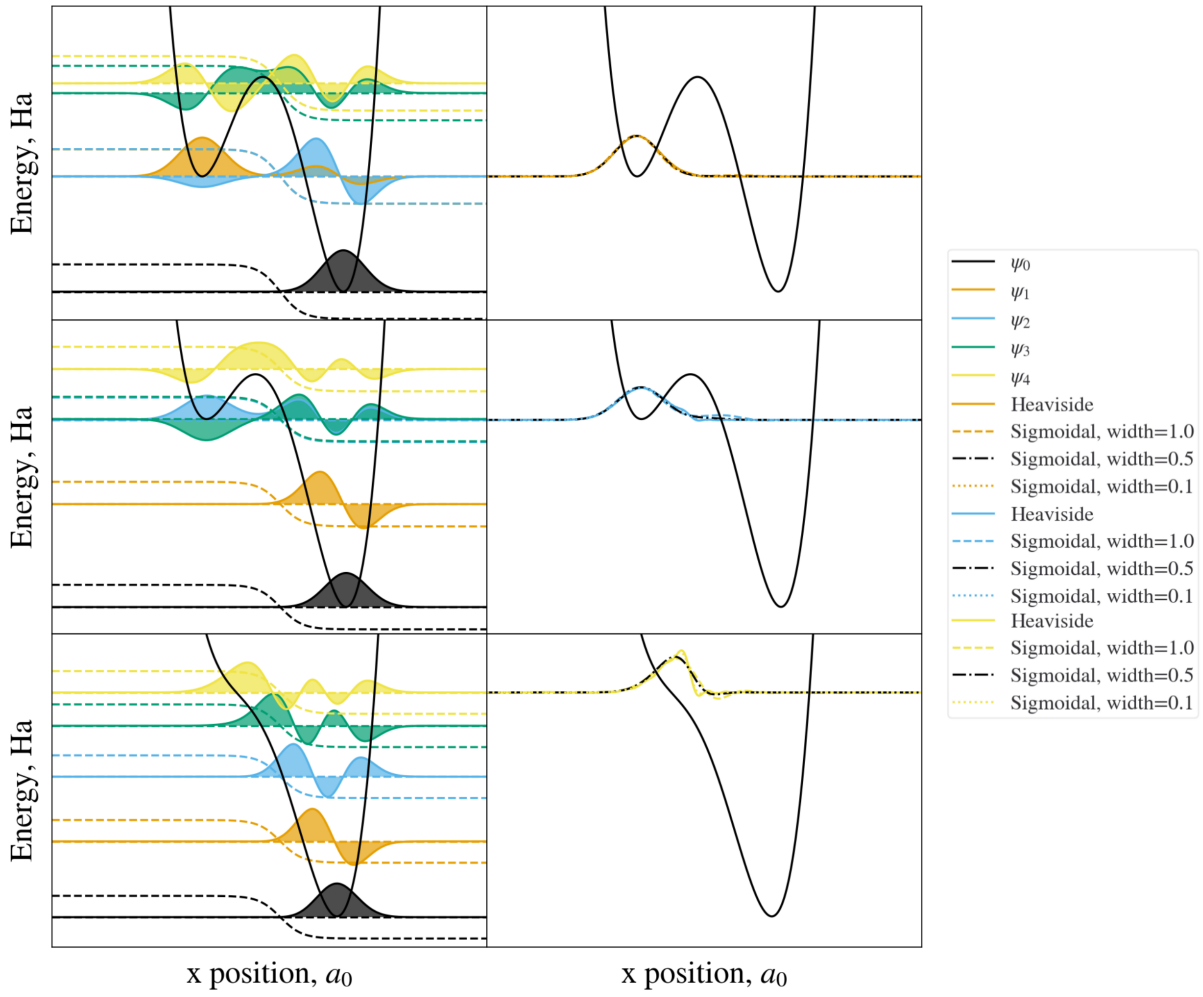

Figure 2: Initial state selection for three different values of ϵ_1, ϵ_2 by applying a sigmoidal or Heaviside filtering function. The procedure is illustrated for the first 5 eigenstates, plotted with the metapotential on the background to showcase how the localization scheme performs. The right side showcases the effect of the different filter parameters as applied to the most suitable state that contains more than 50% density on the top well. Higher values of the sigmoidal tail value reduce initial state localization, while higher values introduce oscillatory motions due to the verticality of the filter function near its center.

Dynamics Subspace

The accuracy of the dynamics is dependent on the number of Fock basis states used. However, the size of the Lindbladian matrix scales as $\mathcal{O}(N^4)$ with the number of Fock states as compared to the Hamiltonian $\mathcal{O}(N^2)$, which makes matrix exponentiation (performed once for each set of Hamiltonian parameters) and multiplication (performed for each timestep in a trajectory) a limiting factor in simulation. Thus, we generate the complete Hamiltonian with a large number of Fock states (N=300) and numerically diagonalize to obtain accurate eigenvalues and eigenvectors and use the first M=20 states to perform a similarity transformation matrix to reduce the dynamics computational space:

$$H_{N\times N}C_{N\times N} = \lambda_{N\times N}C_{N\times N} \rightarrow D_{N\times M} \equiv C_{N\times M} \tag{26}$$

Where $\lambda_{N\times N}$, $C_{N\times N}$ contains the eigenvalues, eigenvectors of the Hamiltonian $H_{N\times N}$ in the full N-dimensional space and $C_{N\times M}$ represent the reduced dimensionality eigenvector matrix containing the first M eigenstates which is defined as the transformation matrix $D_{N\times M}$. Then the initial state ($\hat{\rho}_0$), the Hamiltonian (H) and the Lindbladian ladder operators ($a^\dagger, a$) are transformed into the reduced Hilbert space according to the transformation,

$$A'_{M\times M} = D^T_{M\times N}A_{N\times N}D_{N\times M} \tag{27}$$

As a consequence of this, the ladder operators now encode information about the properties of the Hamiltonian and thus can better simulate the dynamics of the system.

Observables

For this work, we focus on observables corresponding to traces with the time-evolved state. These include traces with the initial state corresponding to the lowest-lying state on the initial well, $\mathrm{Tr}\{\hat{\rho}_t\hat{\rho}_0\}$, and traces with the Heaviside function to obtain the population on

the right side, $P_R = \mathrm{Tr}\{\hat{\rho}_t \Theta(x; x_0)\}$ or traces with the complement of the Heaviside function to obtain the population on the left, $P_L = \mathrm{Tr}\{\hat{\rho}_t (1 - \Theta(x; x_0))\}$. Finally, we look at the eigenvalues obtained by exact diagonalization of the Lindbladian to assess the principal modes/mechanisms of population transfer as well as the long-time final equilibrium state. We focus on the maximum amplitude non-zero real eigenvalue, to compute the decay time defined as follows:

$$T_X = -[\Re\lambda]^{-1} \tag{28}$$

which represents the slower decaying timescale of the Lindbladian. Note that this gives qualitative insight into the relaxation rate, while bypassing the more expensive requirement of performing dynamics propagation.

Simulating barrier crossing dynamics on a Kerr-cat device

Barrier crossing dynamics of the type typically observed in chemical systems requires coupling the reaction coordinate to a bath of non-reactive DOFs which acts both as an energy source for activating the chemical system from the bottom of the reactant well to the vicinity of the barrier top and as an energy sink for stabilizing the system in the product well once barrier crossing occurred. Since the Kerr-cat Hamiltonian in Eq. (2) only describes the dynamics along the reaction coordinate, treating it as a closed quantum system undergoing unitary dynamics would not generate the desirable chemical dynamics. Coupling the reaction coordinate to a thermal bath of nonreactive DOFs takes us to the domain of *nonunitary* open quantum systems dynamics. In what follows, we will assume that this dynamics is described by the following Lindblad quantum master equation:

$$\frac{\partial\hat{\rho}(t)}{\partial t} = -\frac{i}{\hbar}\left[\hat{H}_{\mathrm{KC}},\hat{\rho}(t)\right] \tag{29}$$

$$+\kappa\left(1+n_{\mathrm{th}}\right)\left[\hat{a}\hat{\rho}(t)\hat{a}^{\dagger}-\frac{1}{2}\left\{\hat{a}^{\dagger}\hat{a},\hat{\rho}(t)\right\}\right] \tag{30}$$

$$+\kappa n_{\mathrm{th}}\left[\hat{a}^{\dagger}\hat{\rho}(t)\hat{a}-\frac{1}{2}\left\{\hat{a}\hat{a}^{\dagger},\hat{\rho}(t)\right\}\right]$$

$$\equiv\mathcal{L}\hat{\rho}(t). \tag{31}$$

$$\tag{32}$$

Here, $\hat{\rho}(t)$ is the density operator that describes the state of the reactive system, $\hat{H}_{KC}$ is the Kerr-cat Hamiltonian of the reactive system [Eq. (2)], $\{\kappa n_{\mathrm{th}},\kappa(n_{\mathrm{th}}+1)\}$ are parameters that determine the rates of bath-induced uphill and downhill transitions, respectively, and thereby the coupling strength between the reaction coordinate and the bath of non-reactive DOFs and $\mathcal{L}$ is the Lindbladian superoperator.

Simulating the dissipative dynamics described by Eq. (32) was accomplished by vec-

torizing the density operator and matricizing the Lindbladian superoperator, followed by diagonalizing $\mathcal{L}$ and propagating the vectorized density operator according to

$$\hat{\rho}(t) = e^{\mathcal{L}t}\hat{\rho}(0) \quad . \tag{33}$$

The initial state was chosen so that it is localized in the reactant well. To this end, we picked the first eigenstate of the Kerr-cat Hamiltonian with more than 50% probablity of being in the reactant well and then multiplied it by a sigmoidal function that filtered out the part of the wave function that resides in the product well. Given this reactant-well-localized wave function, $|\psi_R\rangle$, the initial density operator is given by $\hat{\rho}(0) = |\psi_R\rangle\langle\psi_R|$ (a pure state).

The barrier crossing rate constant is given by $k = 1/T_X$, where T_X defines the barrier crossing time scale. T_X was determined in two ways:

1. As the inverse of the maximum amplitude non-zero real eigenvalue of the Lindbladian supermatrix, obtained via diagonalization, as in figure 3a.

2. As the time scale of decay of $Tr\left[\hat{\rho}_t\Theta_X\right]$, obtained via fitting to an exponential, as in figure 3 (b).

The two methods for determining T_X gave similar results and were found to exhibit the same behavior when it comes to the dependence of T_X on the Kerr-cat parameters. The results reported in the text were obtained via method 1 unless otherwise noted (figure 3b).

The following analysis is for the case of $\Delta = 0$, and using the convention $\hbar = 1$ and K as a unit of energy. A complete description of the methodology is included in Computational Methods.

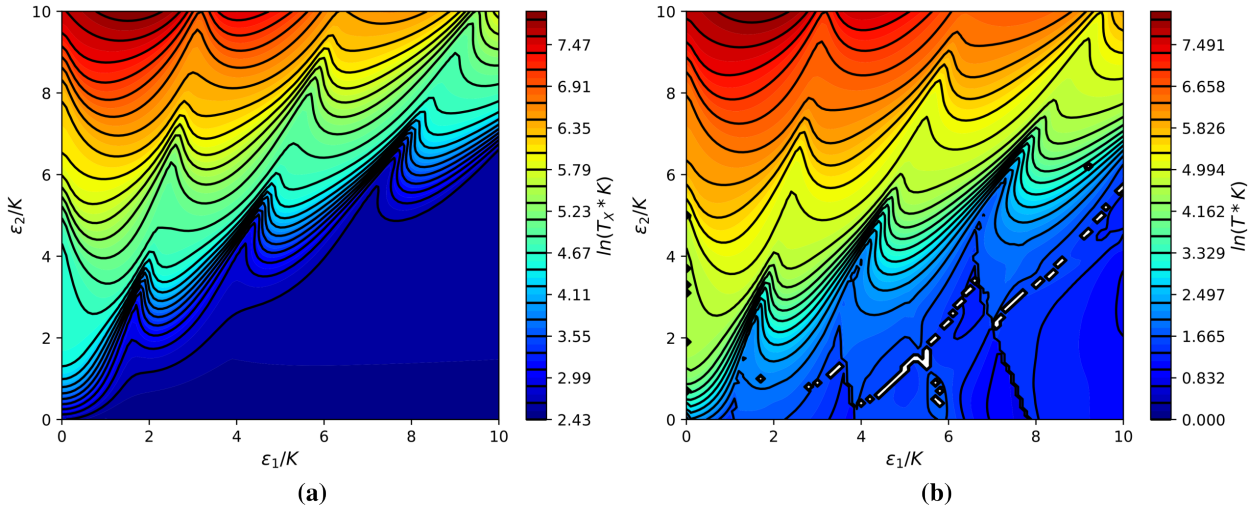

Figure 3: Relaxation timescales associated with the (a) Lindbladian maximal real eigenvalue (left) and (b) the dynamical relaxation rates (right) obtained by fitting the population traces as a function of the Kerr-cat parameters ϵ_1 and ϵ_2. Both plots use dissipation parameters $\kappa = 0.1$, $n_{\text{th}} = 0.1$.

The dependence of T_X on the Kerr-cat parameters ϵ_1 and ϵ_2 is shown in Fig. 3. The plot shows a rich structure including (a) a zone in the lower right corner where the barrier crossing is very fast, which corresponds to a low barrier or a complete lack of a barrier, (b) Fast barrier crossing in the upper left corner for particular values of (ϵ_1, ϵ_2) where the energy levels in the reactant and product wells are in resonance (see white lines in Figs. 3 and SI), and (c) alternation between "broad" and "thin" resonance transitions both as a function of ϵ_1 for fixed ϵ_2 and along the (ϵ_1, ϵ_2) resonance line.

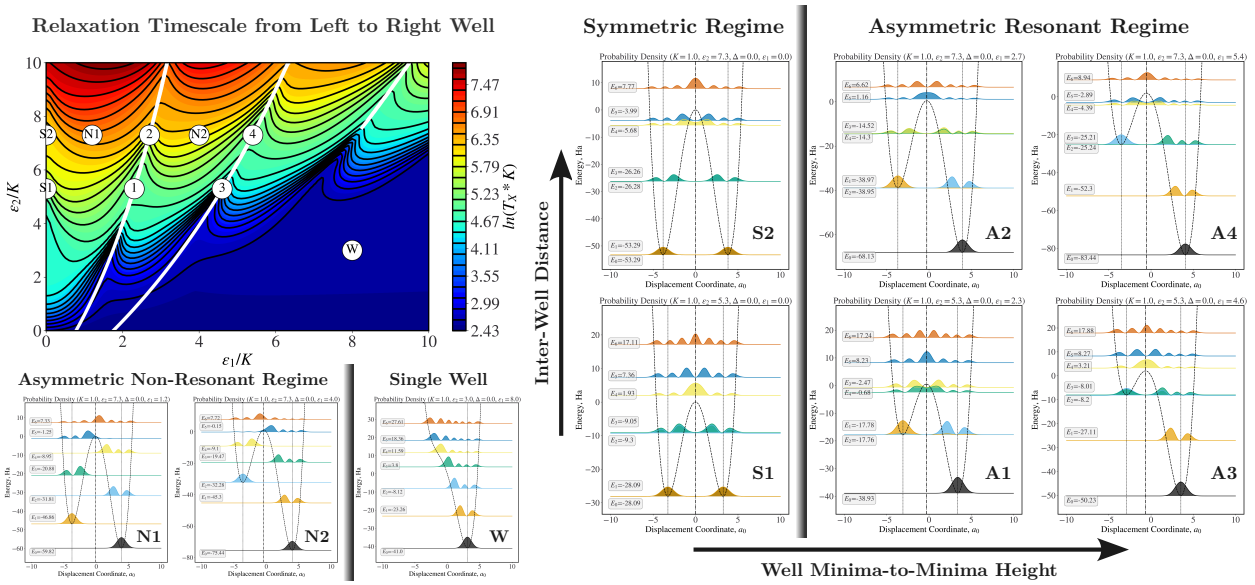

Figure 4: Resonant and non-resonant regimes of the eigendensities between both sides of the double-well along the $p = 0$ metapotential cut. Each state are plotted as a function of position superimposed on the metapotential cut spanning $x \in [-10, 10]$ Bohr. The vertical axis denotes the absolute energy obtained by diagonalizing the Hamiltonian. Panels include the asymmetric non-resonant regime (N1, N2), a region where the double-well description is no longer valid (W). The resonant regime falls along the white lines and reflect regimes with no asymmetry (S1, S2) as well as regions of increasing well asymmetry (A1-A2, A3-A4) by changing the minima-to-minima height.

The fast barrier crossing regimes correspond to resonances between the energy levels in the reactant and product wells which lead to efficient tunneling through the barrier. The aforementioned "thin" regions correspond to eigenstate overlap near the top of the barrier as well as a high state density at the barrier top, providing a transient state to retain population before decaying to the global ground state (see figure 3 and corresponding panels S1, 2, 3 of figure 4). By contrast the "broad" regimes contain degenerate states but no density centered at the top of the barrier, thus reducing the overall population transfer rate (see figure 3 and corresponding panels S2, 1, 4 of figure 4). However, the rate is nonetheless enhanced due to the presence of quasi-degenerate states near the barrier top, providing a pathway for barrier crossing. Furthermore, the intermediate states without resonant states have longer lifetimes due to lack of overlap between eigenstates or localized state density on either side of the well (see figure 3 and corresponding panels N1 and N2 of figure 4). Going along each of the

resonance lines showcases an increasing number of degenerate pairs of states with increasing ϵ_2 (figure 3: S1-S2; 1-2; 3-4). Going between different resonance lines with increasing ϵ_1 changes the first state index in resonance between the two wells (S1: first and second, 1: second and third, 3: third and fourth).

Finally, a decrease in the minimum-to-minimum height decreases the barrier height until the double-well is destroyed (figure 4, W). This decreases the relaxation lifetime as the kinetics driving the process is merely vertical de-excitation to the ground state. Although there can be a relaxation timescale associated with the process this is not a measurement of the kinetics of population transfer between the wells, as this is an ill-defined process in this parameter regime.

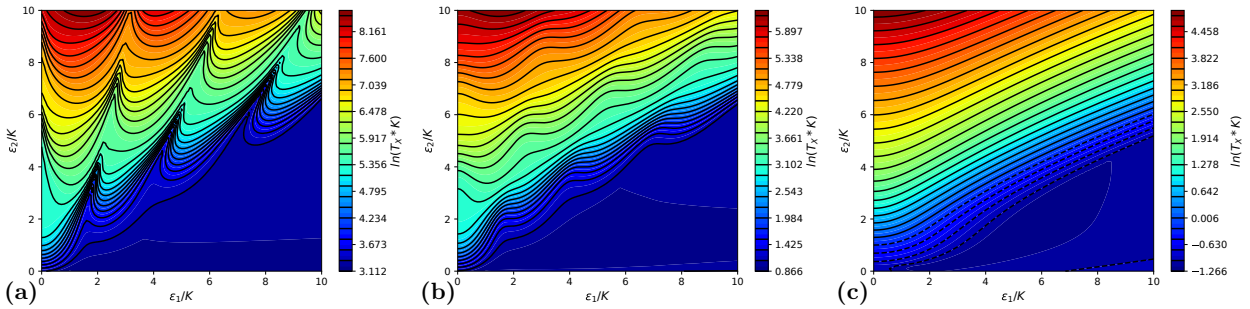

Figure 5: Dependence of timescale obtained by exact Lindbladian diagonalization on the dissipation parameter κ, for $n_{\text{th}} = 0.1$. (a) $\kappa = 0.05$. (b) $\kappa = 0.5$. (c) $\kappa = 5.0$.

Fig. 5 shows how the dependence of T_X on ϵ_1 and ϵ_2 is impacted by the the strength of coupling between the reaction coordinate and the bath of nonreactive DOFs, as measured by κ. As expected, T_X shows an overall trend of increasing with decreasing coupling strength, which can be traced back to the fact that the rate of activation from the bottom of the reactant well to to the vicinity of the barrier top and stabilization in the product well after barrier crossing are determined by κ. Additionally, the dependence of T_X on ϵ_1 and ϵ_2 is seen to become less structured with increasing κ, which can be traced back to ability of dissipation to wash out resonance effects. More specifically, while tunnelling dominates the kinetics at low values of κ, classical-like barrier crossing and thereby TST/Arrhenius-like kinetics is observed at larger values of κ. A more extensive set of data that showcases this

observation for a wider range of parameter regimes is provided in the supporting information.

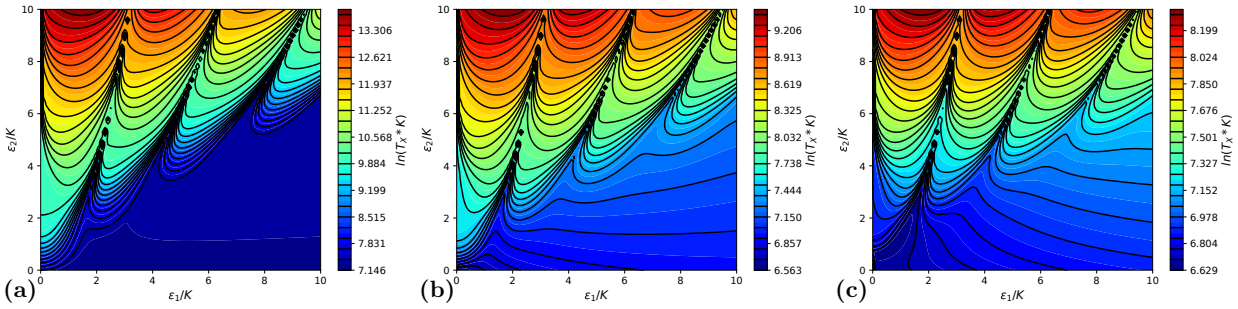

Figure 6: Dependence of timescale obtained by exact Lindbladian diagonalization on the dissipation parameter κ, for $\kappa = 0.001$. (a) $n_{\text{th}} = 0.05$. (b) $n_{\text{th}} = 0.5$. (c) $n_{\text{th}} = 1.0$.

Finally, Fig. 6 shows how the dependence of T_X on ϵ_1 and ϵ_2 is impacted by the bath temperature, as measured by n_{th}. While T_X shows an overall increase with decreasing n_{th}, the structure is seen to be minimally impacted by changing n_{th}.

Basis Set Convergence

In this section, we explore the convergence of the Kerr-cat Hamiltonian parameters to the number of Eigen-basis used. In Fig. 7, we present the timescales obtained from the exact diagonalization of the Lindbladian as a function of Hamiltonian parameters ϵ_1 and ϵ_2, for a different number of Eigen-basis. As can be appreciated, with $n_{basis} > 10$ the timescales are semi-quantitative converged, and with $n_{basis} > 20$ quantitative agreement is found. Unless otherwise stated, we used $n_{basis} = 20$ for the device dynamics.

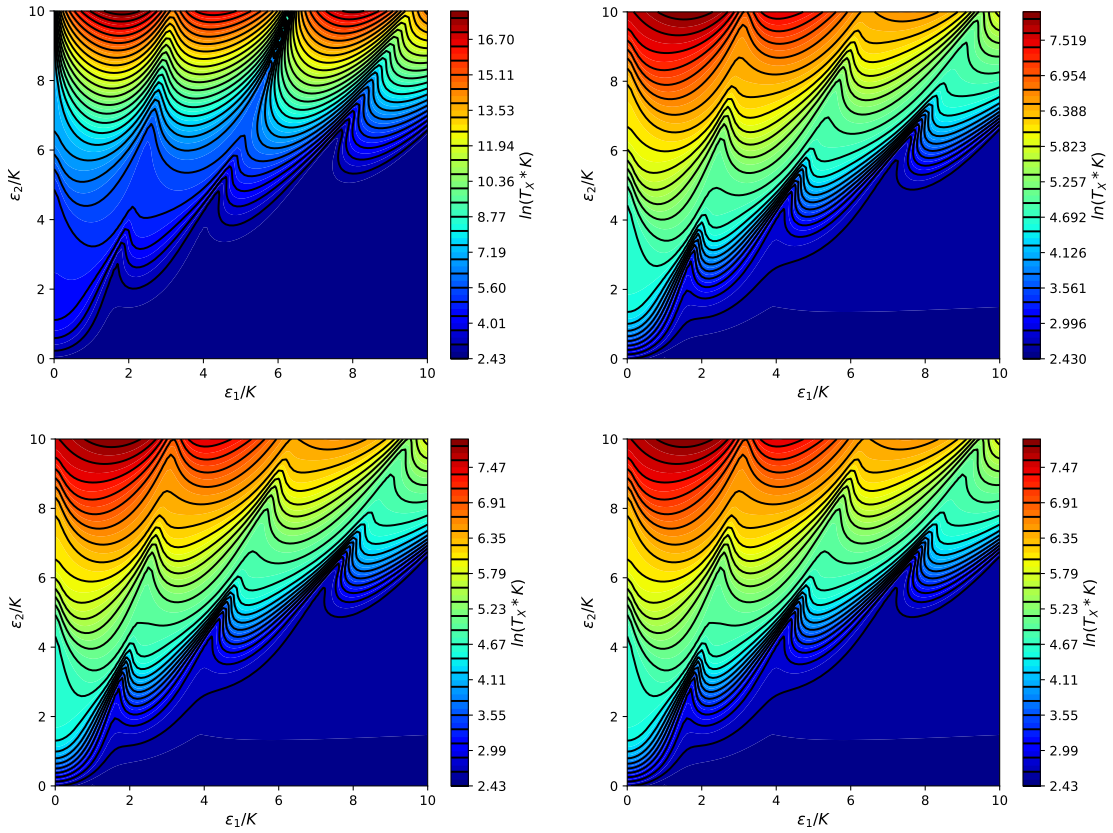

Figure 7: Convergence of Lindbladian eigenvalue timescale as a function of the number of Eigen-basis. (a) $n_{basis} = 5$. (b) $n_{basis} = 10$. (c) $n_{basis} = 20$. (d) $n_{basis} = 30$.

Chemical Potentials

The chemical potentials were obtained from the literature, and are listed within the tables in this section.

Table 1: Literature chemical potential parameters given by expression $V_{\text{literature}} = k_1 x - k_2 x^2 - k_3 x^3 + k_4 x^4$

System	k_4	k_3	k_2	k_1	Units
Thymine-Adenine (DNA)[9]	0.02068986	0.00525515	0.0413797	0.0157655	E_h
Malonaldehyde (cis-trans)[10,11]	0.00009374	0.000109	0.00299	0.005232	a.u.
Malonaldehyde (cis-cis)[10,11]	0.000714286	0	0.004	0	a.u.

Table 2: Literature chemical potential parameters given by expression $V_{\text{literature}} = V_1\{\exp(-2a_1[x-r_1]) - 2\exp[-a_1(x-r_1)]\} + V_2\{\exp(2a_2[x-r_2]) - 2\exp[a_2(x-r_2)]\}$

System	V_1	V_2	a_1	a_2	r_1	r_2	Units
Guanine-Cytosine (DNA)[12]	0.1617	0.082	0.305	0.755	-2.7	2.1	a.u.

Furthermore, we note that the adenine-thymine potential is expressed in terms of a unitless length parameter $\zeta = x/x_0$, which has been estimated to be $x_0 = 1.9592\, a_0$ based on matching the energy eigenvalues listed in reference 9. For the dynamics shown in this work, the given literature potentials where fit to the simpler double-well potential, without a cubic polynomial term,

$$\hat{V}_{\text{DW}} = k_4 \hat{x}^4 + k_2 \hat{x}^2 + k_1 \hat{x}_1 \tag{34}$$

Dynamics Trajectories and Rate Fits

This section lists additional trajectory plots for both the double-well and Kerr-cat analog for different values of c and a plot of the resulting fitted rates. These plots cover the dissipation parameters listed in the main text.

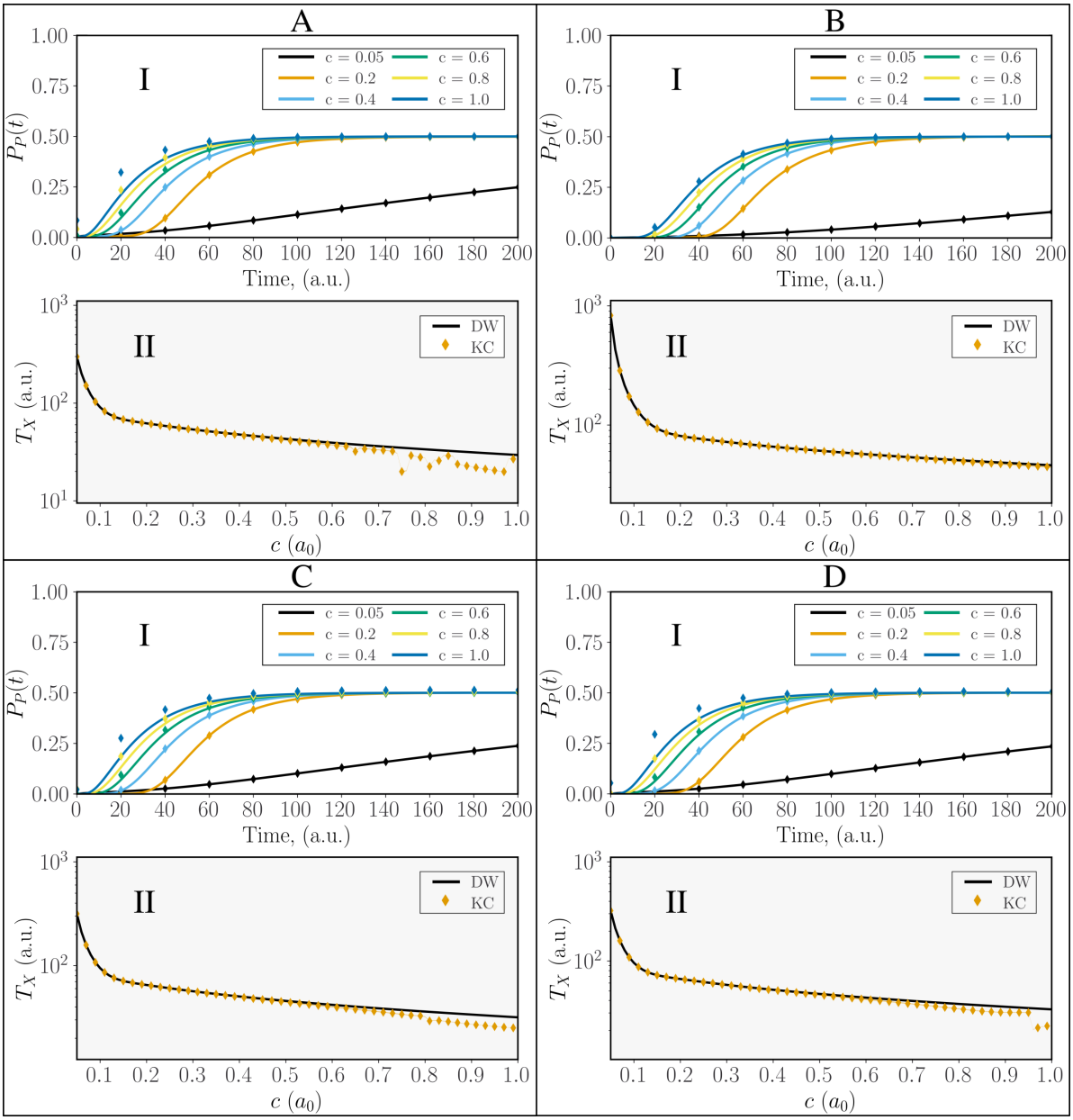

Figure 8: Comparison of observables computed obtained with $\hat{H}_{DW}$ (solid lines) and $\hat{H}_{KC}$ (diamonds) as a function of c, using $\kappa = 0.1$, and $n_{\text{th}} = 0.1$. The time evolution of the product population for the four proton transfer reactions are shown in the top subpanels. The corresponding inverse reaction rate constants are shown in the bottom subpanels.

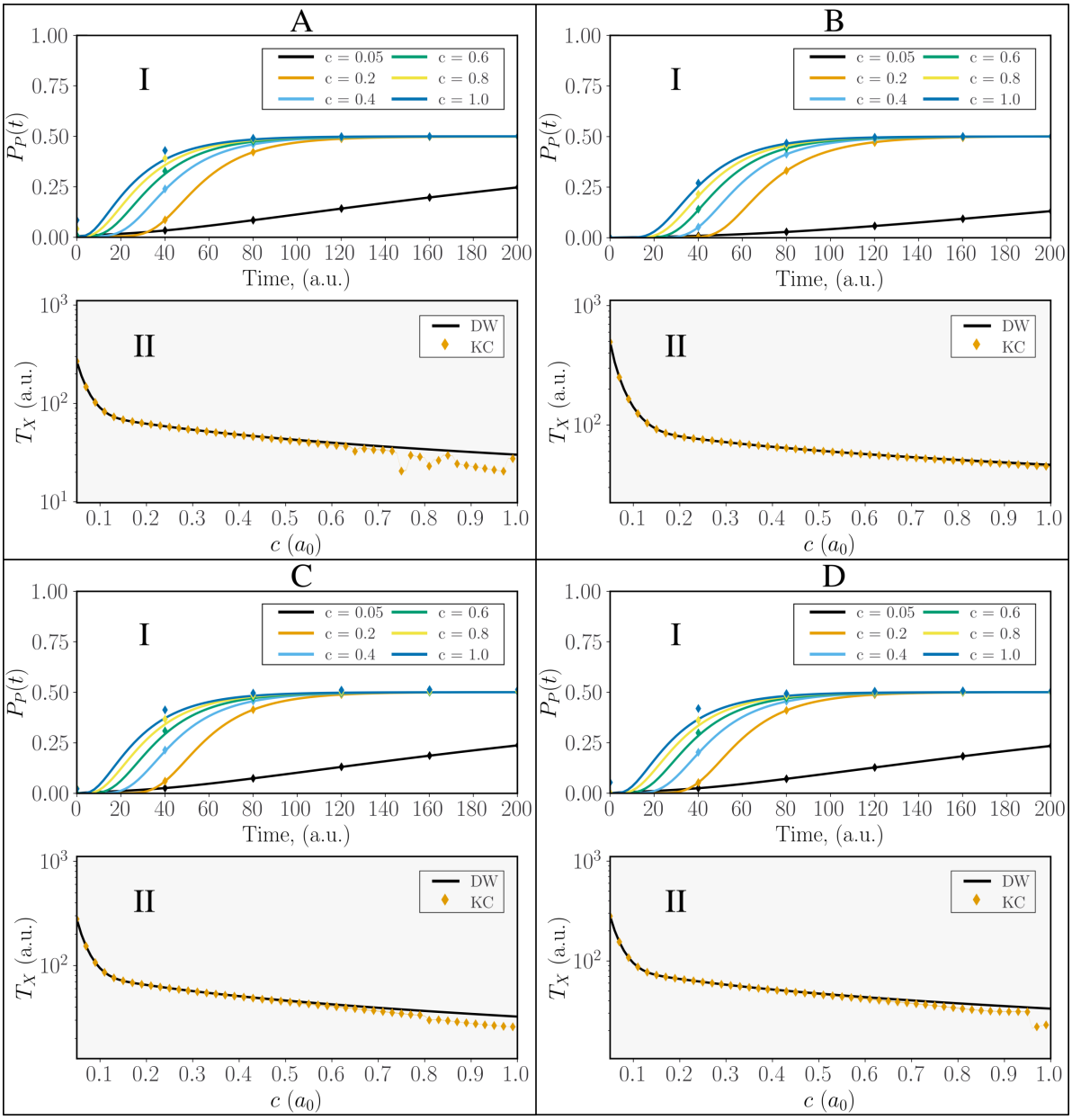

Figure 9: Comparison of observables computed obtained with $\hat{H}_{DW}$ (solid lines) and $\hat{H}_{KC}$ (diamonds) as a function of c, using $\kappa = 0.1$, and $n_{\text{th}} = 0.05$. The time evolution of the product population for the four proton transfer reactions are shown in the top subpanels. The corresponding inverse reaction rate constants are shown in the bottom subpanels.

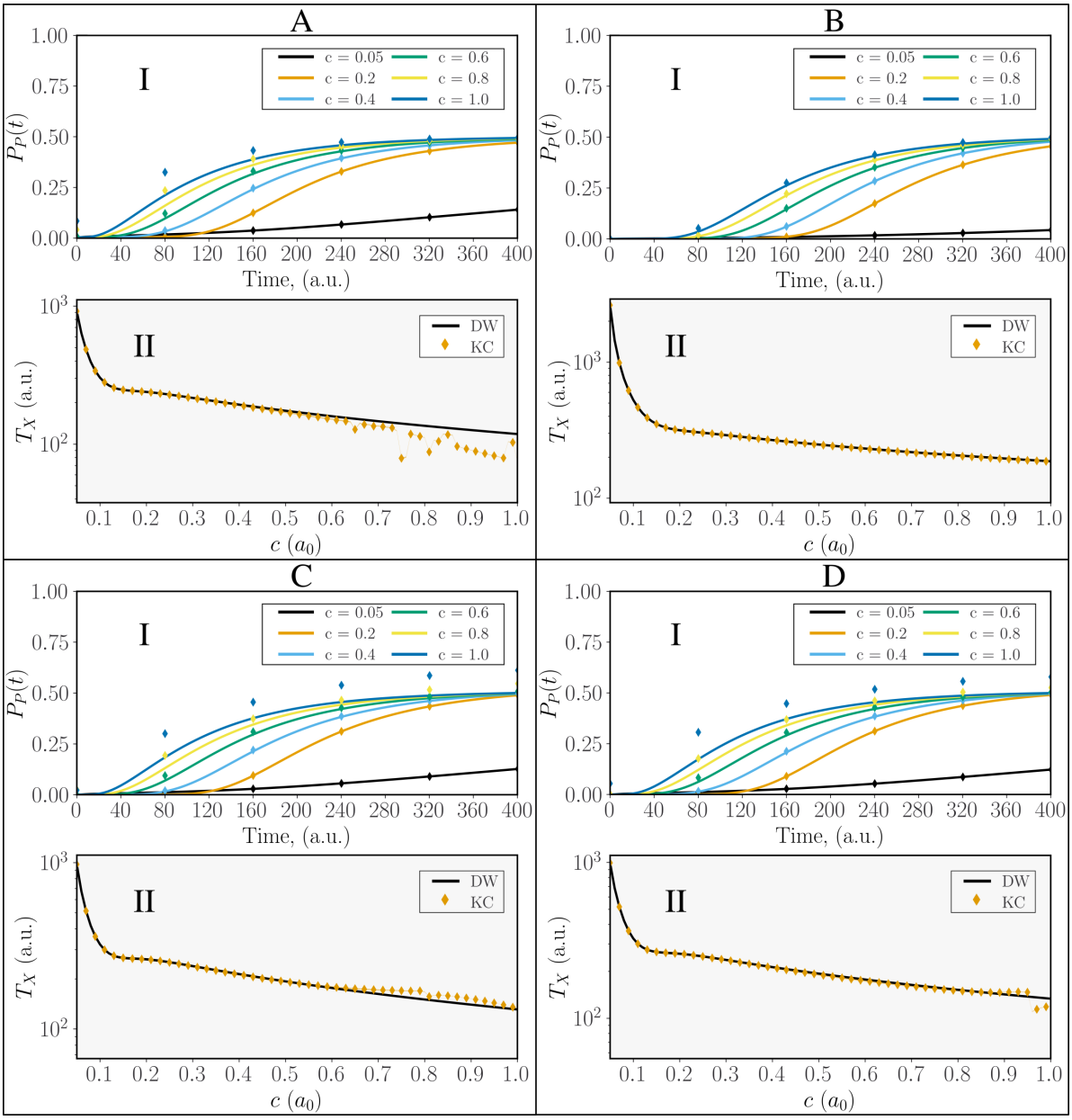

Figure 10: Comparison of observables computed obtained with $\hat{H}_{DW}$ (solid lines) and $\hat{H}_{KC}$ (diamonds) as a function of c, using $\kappa = 0.025$, and $n_{\text{th}} = 0.1$. The time evolution of the product population for the four proton transfer reactions are shown in the top subpanels. The corresponding inverse reaction rate constants are shown in the bottom subpanels.

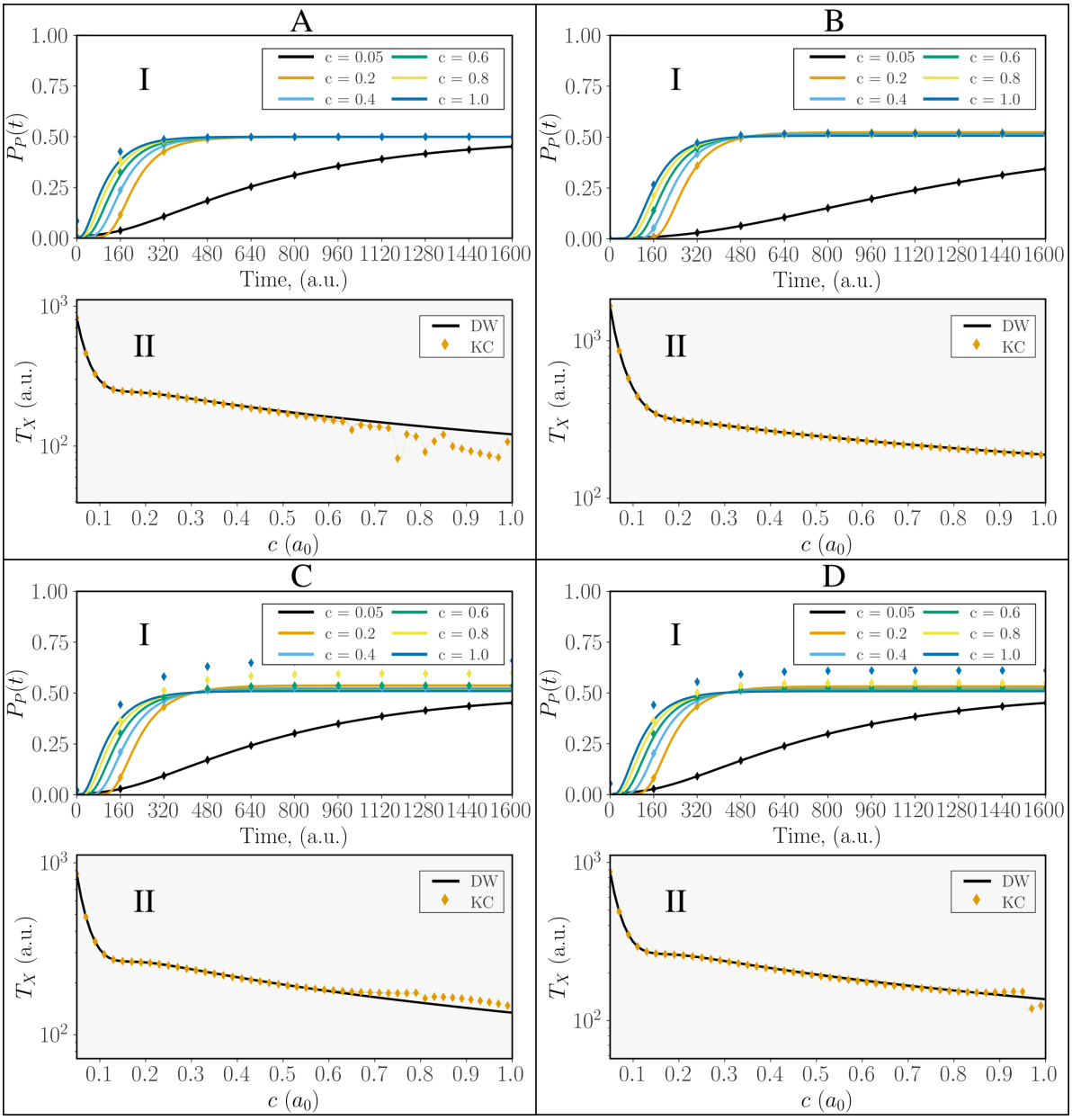

Figure 11: Comparison of observables computed obtained with $\hat{H}_{DW}$ (solid lines) and $\hat{H}_{KC}$ (diamonds) as a function of c, using $\kappa = 0.025$, and $n_{\text{th}} = 0.05$. The time evolution of the product population for the four proton transfer reactions are shown in the top subpanels. The corresponding inverse reaction rate constants are shown in the bottom subpanels.

Basis Benchmark for Dynamical Evolution

This section showcases the dynamics evolution figures for the four systems, using a different number of basis set to showcase the convergence of the results listed in the main text. The figures showcase the results of using a Fock space of dimension 50, 100 and 150 to accurately represent the Hamiltonian and eigenstates, which are then used for the dynamics propagation in a reduced subspace. For all cases, 50 eigenstates were used for the dynamics propagation, which incorporate many levels beyond the barrier top energy. For some of the listed systems, dynamics convergence with respect to number of eigenstates is observed for values much smaller than fifty. Deviations of the Kerr-cat fitted rates at larger c-values result from the Hamiltonian perturbative terms that are sensitive to the value of c and errors associated with the fitting protocol.

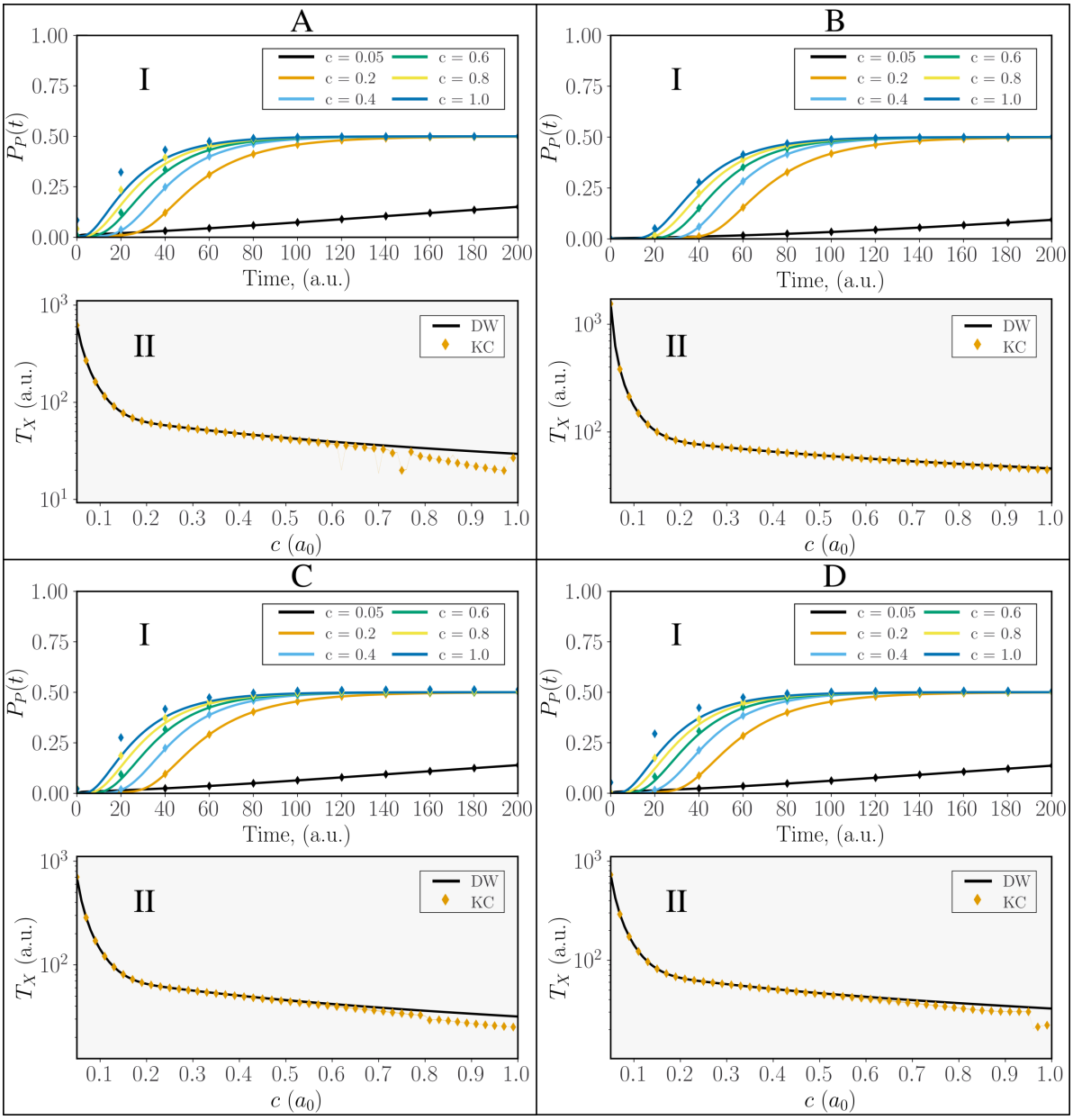

Figure 12: Comparison of observables computed obtained with $\hat{H}_{DW}$ (solid lines) and $\hat{H}_{KC}$ (diamonds) as a function of c, using $\kappa = 0.1$, and $n_{\text{th}} = 0.1$. The time evolution of the product population for the four proton transfer reactions are shown in the top subpanels. The corresponding inverse reaction rate constants are shown in the bottom subpanels. These results were generated using 50 Fock basis for Hamiltonian and initial state preparation and a subspace of 50 eigenfunctions for dynamics propagation.

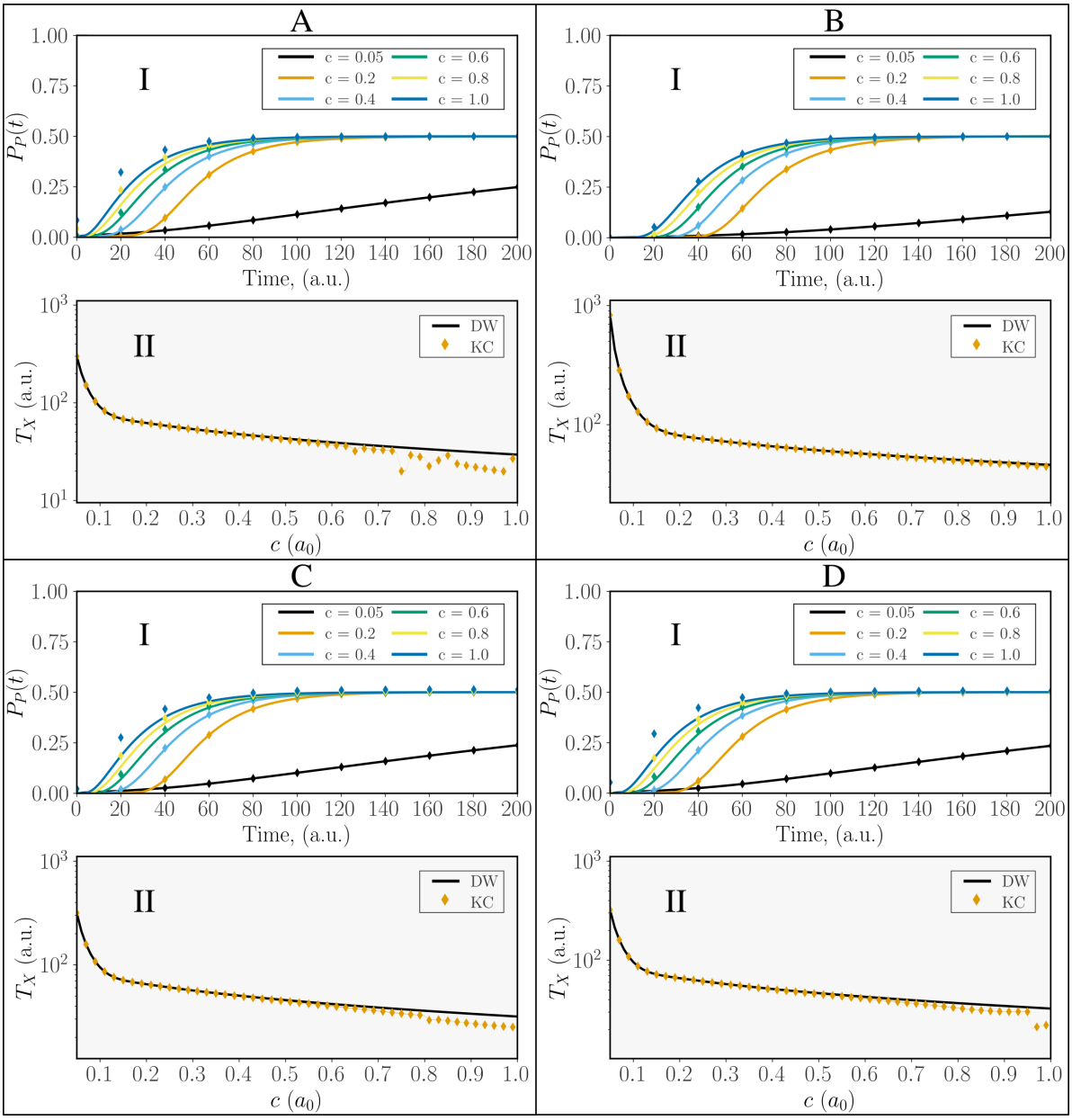

Figure 13: Comparison of observables computed obtained with $\hat{H}_{DW}$ (solid lines) and $\hat{H}_{KC}$ (diamonds) as a function of c, using $\kappa = 0.1$, and $n_{\text{th}} = 0.1$. The time evolution of the product population for the four proton transfer reactions are shown in the top subpanels. The corresponding inverse reaction rate constants are shown in the bottom subpanels. These results were generated using 100 Fock basis for Hamiltonian and initial state preparation and a subspace of 50 eigenfunctions for dynamics propagation.

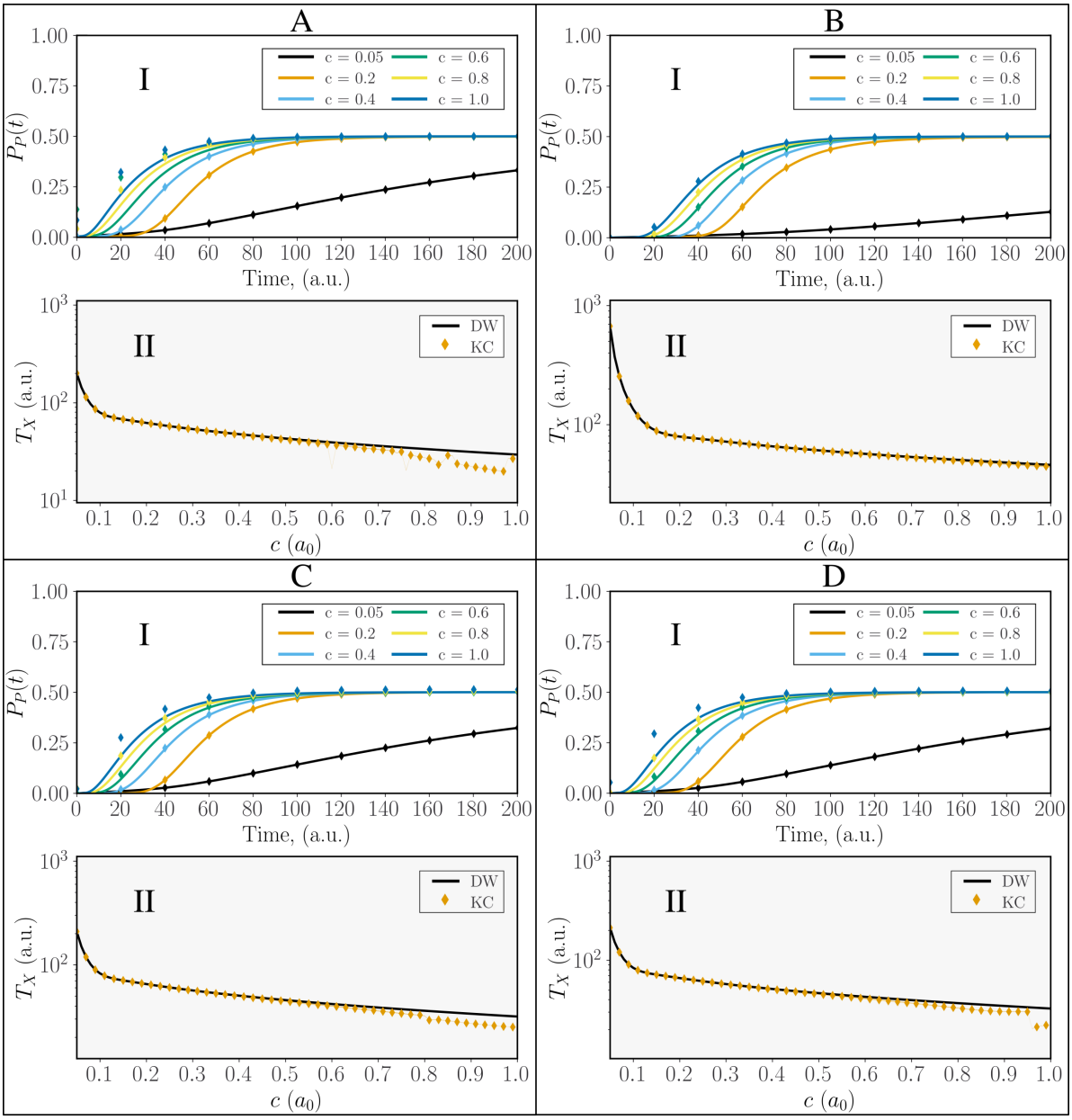

Figure 14: Comparison of observables computed obtained with $\hat{H}_{DW}$ (solid lines) and $\hat{H}_{KC}$ (diamonds) as a function of c, using $\kappa = 0.1$, and $n_{\text{th}} = 0.1$. The time evolution of the product population for the four proton transfer reactions are shown in the top subpanels. The corresponding inverse reaction rate constants are shown in the bottom subpanels. These results were generated using 150 Fock basis for Hamiltonian and initial state preparation and a subspace of 50 eigenfunctions for dynamics propagation.

References

(1) Vazquez, F. X.; Talapatra, S.; Sension, R. J.; Geva, E. The Entropic Origin of Solvent Effects on the Single Bond *cZt-tZt* Isomerization Rate Constant of 1,3,5- *cis* -Hexatriene in Alkane and Alcohol Solvents: A Molecular Dynamics Study. *J. Phys. Chem. B* **2014**, *118*, 7869–7877.

(2) Frattini, N. E.; Cortiñas, R. G.; Venkatraman, J.; Xiao, X.; Su, Q.; Lei, C. U.; Chapman, B. J.; Joshi, V. R.; Girvin, S. M.; Schoelkopf, R. J. et al. Observation of Pairwise Level Degeneracies and the Quantum Regime of the Arrhenius Law in a Double-Well Parametric Oscillator. *Phys. Rev. X* **2024**, *14*, 031040.

(3) Venkatraman, J.; Cortinas, R. G.; Frattini, N. E.; Xiao, X.; Devoret, M. H. A driven quantum superconducting circuit with multiple tunable degeneracies. *arXiv:2211.04605* **2023**, http://arxiv.org/abs/2211.04605 (accessed 2023-11-13).

(4) Reynoso, M. A. P.; Nader, D. J.; Chávez-Carlos, J.; Ordaz-Mendoza, B. E.; Cortiñas, R. G.; Batista, V. S.; Lerma-Hernández, S.; Pérez-Bernal, F.; Santos, L. F. Quantum tunneling and level crossings in the squeeze-driven Kerr oscillator. *Phys. Rev. A* **2023**, *108*, 033709.

(5) Chávez-Carlos, J.; Lezama, T. L. M.; Cortiñas, R. G.; Venkatraman, J.; Devoret, M. H.; Batista, V. S.; Pérez-Bernal, F.; Santos, L. F. Spectral kissing and its dynamical consequences in the squeeze-driven Kerr oscillator. *npj Quantum Inf.* **2023**, *9*, 76.

(6) Iachello, F.; Cortiñas, R. G.; Pérez-Bernal, F.; Santos, L. F. Symmetries of the squeeze-driven Kerr oscillator. *J. Phys. A* **2023**, *56*, 495305.

(7) Gonzalez, D.; Chávez-Carlos, J.; Hirsch, J. G.; Vergara, J. D. Parameter space geometry of the quartic oscillator and the double-well potential: classical and quantum description. *Phys. Scr.* **2024**, *99*, 025247.

(8) Al-Mohy, A. H.; Higham, N. J. A New Scaling and Squaring Algorithm for the Matrix Exponential. *SIAM J. Matrix Anal. Appl.* **2010**, *31*, 970–989.

(9) Godbeer, A. D.; Al-Khalili, J. S.; Stevenson, P. D. Modelling proton tunnelling in the adenine–thymine base pair. *Phys. Chem. Chem. Phys.* **2015**, *17*, 13034–13044.

(10) Ghosh, S.; Bhattacharyya, S. P. Dynamics of atom tunnelling in a symmetric double well coupled to an asymmetric double well: The case of malonaldehyde#. *J. Chem. Sci.* **2012**, *124*, 13–19.

(11) Ghosh, S.; Talukder, S.; Sen, S.; Chaudhury, P. Optimised polychromatic field-mediated suppression of H-atom tunnelling in a coupled symmetric double well: two-dimensional malonaldehyde model. *Mol. Phys.* **2015**, *113*, 3826–3838.

(12) Slocombe, L.; Sacchi, M.; Al-Khalili, J. An open quantum systems approach to proton tunnelling in DNA. *Commun. Phys.* **2022**, *5*, 109.